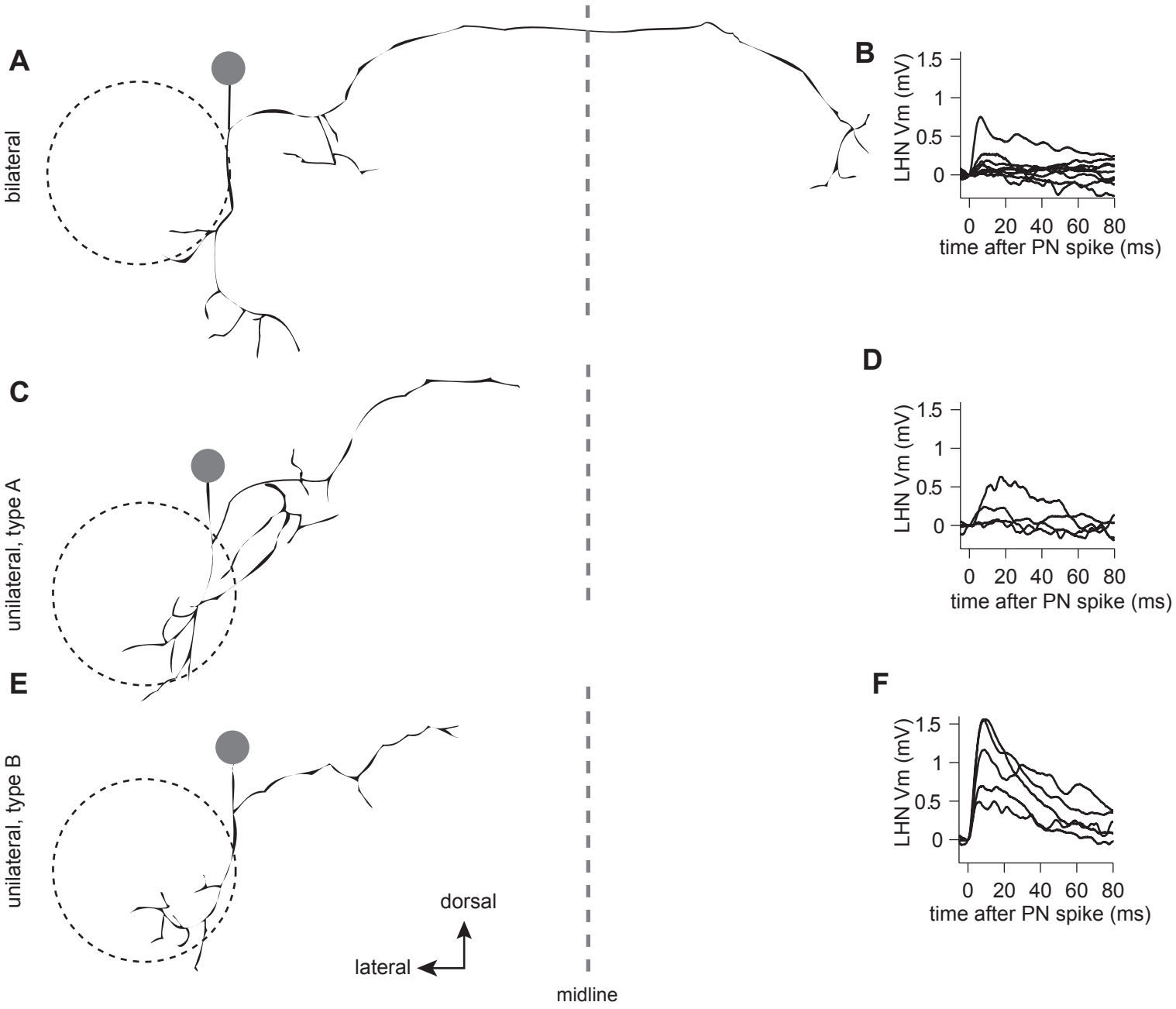

Figure S1 (Related to Figure 5). LHN morphological subtypes and synaptic connectivity with DA1 PNs

All LHN recordings were performed with biocytin in the patch pipette to fill the cell's processes. LHN morphology was then visualized with confocal microscopy and reconstructed with ImageJ software. We recorded LHNs from the cluster known as aSP-f (alternatvely, aSP5 or DC1). We found that the LHN in this cluster comprised three distinct morphologies, which conformed to previous descriptions (Kohl et al., 2013; Ruta et al., 2010). One morphology extended processes bilaterally (**A**; dashed circle denotes lateral horn neuropil). We found a connection in only 1 out of 9 paired recordings with an LHN of this subtype and a DA1 PN (**B**). We term these bilateral LHNs. A second morphology had two processes entering the lateral horn (separated in the anterior-posterior axis) and was strictly unilateral (**C**). We found a connection in only 1 out of 4 paired recordings with an LHN of this subtype and a DA1 PN (**D**). We term these unilateral type A LHNs. A third morphology had one relatively large-diameter process entering the lateral horn and was strictly unilateral (**E**). We found a connection in 5 out of 5 paired recordings with an LHN of this subtype and a DA1 PN (**F**). We term these unilateral type B LHNs. All LHNs reported in the main text are of the unilateral type B morphology.

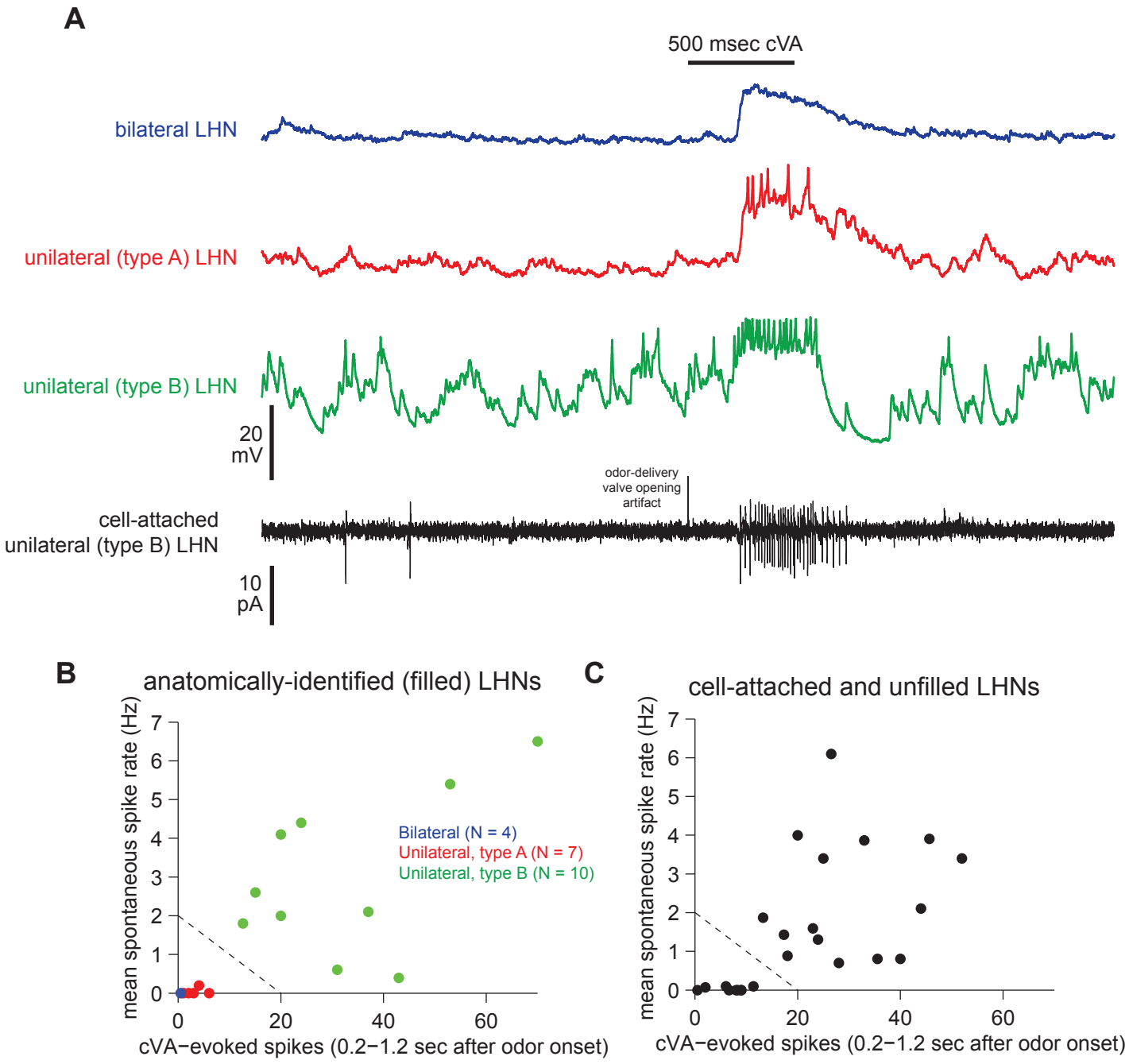

Figure S2 (Related to Figure 1). LHN subtype classification based on physiology

Unilateral type B LHNs could be reliably distinguished from the other LHN types in the same cluster based on physiological criteria. Unilateral type B LHNs had much higher spontaneous firing rates than the other two types, and also stronger responses to cis-vaccenyl acetate (cVA), the best ligand for DA1 ORNs (**A**). These physiological properties were consistent across all anatomically identified LHNs (**B**). (Note: two anatomically identified unilateral type B LHNs were omitted from this analysis because cVA was not presented.) Based on spontaneous firing rates and cVA-evoked firing rates, it is possible for a linear classifier to distinguish unilateral type B LHNs from other LHNs (dashed line in **B**). We also recorded from some LHNs in cases where anatomical data was not available; these cases were either cell-attached recordings (bottom trace in **A**) or else whole-cell recordings that did not yield interpretable fills. To determine which of these "anatomically unidentified" LHNs were of unilateral type B, we applied the same linear classifier (**C**). Thus, all LHNs with sufficiently high spontaneous activity and cVA responsiveness were deemed unilateral type A.

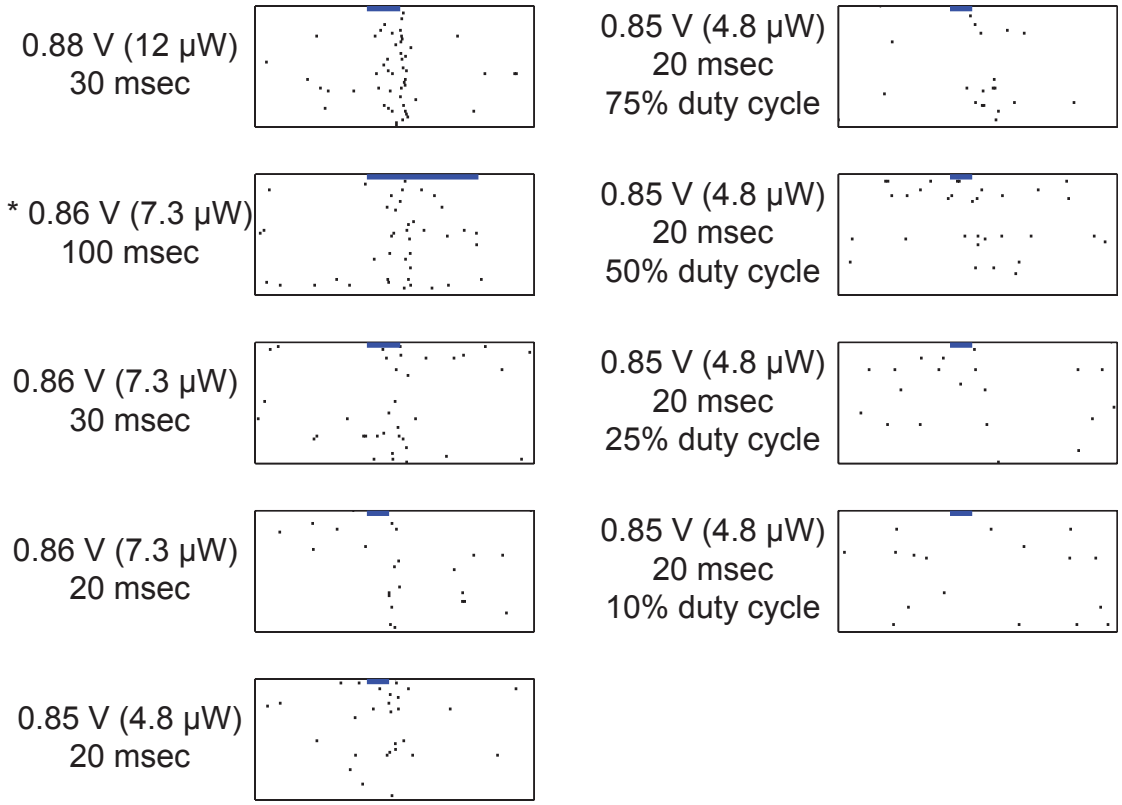

Figure S3 (Related to Figures 1 and 2). Example ORN spike rasters for extended range of stimulus intensities

To generate the gain plots in Figure 1C,D, we presented multiple stimuli with a range of intensities. Each panel shows spiking responses of a typical ORN to each of those stimuli. The blue bar shows the stimulus period. The voltage command to the LED control circuitry and measured LED light output are noted in each case, as is the duration of stimulation. For the four weakest stimuli (right column), the voltage command to the LED control circuitry was flickered at a rate of 500 Hz, and we modulated the duty cycle within this periodic signal. The second stimulus from the top in the left column, marked with an asterisk, is the stimulus used for all other analyses in this study.

For simplicity and consistency, we use one stimulus throughout this study, but we found that other stimuli in the near-threshold regime produced qualitatively similar results. However, it is important to note that these results (particularly the comparison shown in Figure 2B) will be different for strong stimuli. Strong stimuli elicit neural signals which are unambigously separated from neural noise. In this regime, stimulus detection is fast and accurate, even for an observer of a single ORN. Due to the transmission delay between ORNs and PNs, PN accuracy (d') actually lags ORN accuracy when the stimulus is strong (data not shown). Our interest is in studying the regime where stimulus detection is actually challenging.

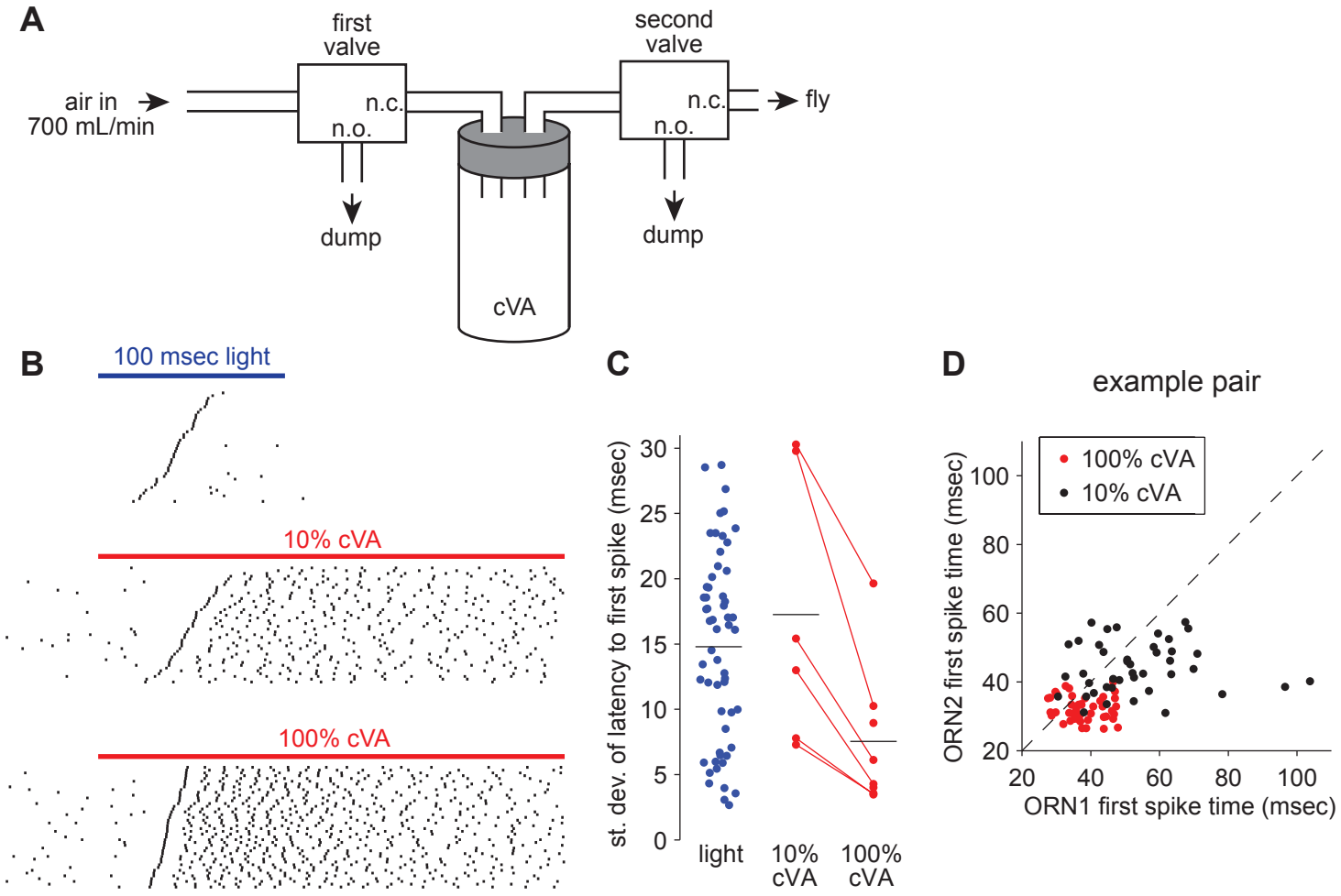

Figure S4 (Related to Figure 1). An optogenetic stimulus can mimic onset of odor stimulation in DA1 ORNs

In this study, we devised an optogenetic approach to injecting a temporally-precise packet of spikes into the DA1 ORN population. Here we show that the onset of an odor can elicit a similar pattern of spiking in DA1 ORNs. The primary ligand for DA1 ORNs is cis-vaccenyl acetate (cVA; Clyne et al., 1997; van der Goes van Naters & Carlson, 2007). To deliver this odor, we used a two-valve device (**A**). The first valve (STV-3-1/4UKG, Takasago Electric, Inc.) was opened to establish a continuous flow of air through the odor vial. The second valve (LFAA1201610H, The Lee Company) was selected for its fast response time, and functioned to turn the flow of odorized air to the fly on or off. In each trial, the first valve opened first, and then 200-400 ms later, the second valve opened for 250-400 ms, and finally both valves were closed.

We found that the odor stimulus was able to produce reliable odor-evoked spiking in ORNs. This was true for both undiluted cVA or cVA diluted to 10% in paraffin oil (**B**). For the 10% cVA stimulus, the precision of the first odor-evoked spike was as high as the precision of the first light-evoked spike for the primary optogenetic stimulus in this study (**B,C**). For the 100% cVA stimulus, the precision of the first odor-evoked spike was even higher than that of the first light-evoked spike (**B,C**). All rasters show trials sorted by first spike latency. ORN first spike latencies were independent in simultaneously-recorded ORNs stimulated with odor (**D**), similar to ORNs stimulated with light (Figure S5). In sum, these data show that the ORN spike patterns produced by our primary optogenetic stimulus can be produced at the onset of odor stimulation as well.

Note that both odor-evoked activity adapts over time (**B**), and light-evoked activity also adapts over time (**Figure 1E**). This may be due to adaptation in ORN spike generation. Alternatively, it may be due to adaptation in channelrhodopsin currents and also adaptation in olfactory transduction currents (Nagel & Wilson 2010).

Clyne, P., Grant, A., O'Connell, R., and Carlson, J.R. (1997). Odorant response of individual sensilla on the *Drosophila* antenna. *Invert. Neurosci.* 3, 127-135.

Nagel, K.I., and Wilson, R.I. (2010) Biophysical mechanisms underlying olfactory receptor neuron dynamics. *Nat. Neurosci.* 14:208-216.

van der Goes van Naters, W., and Carlson, J.R. (2007). Receptors and neurons for fly odors in *Drosophila*. *Curr. Biol.* 17, 606-612.

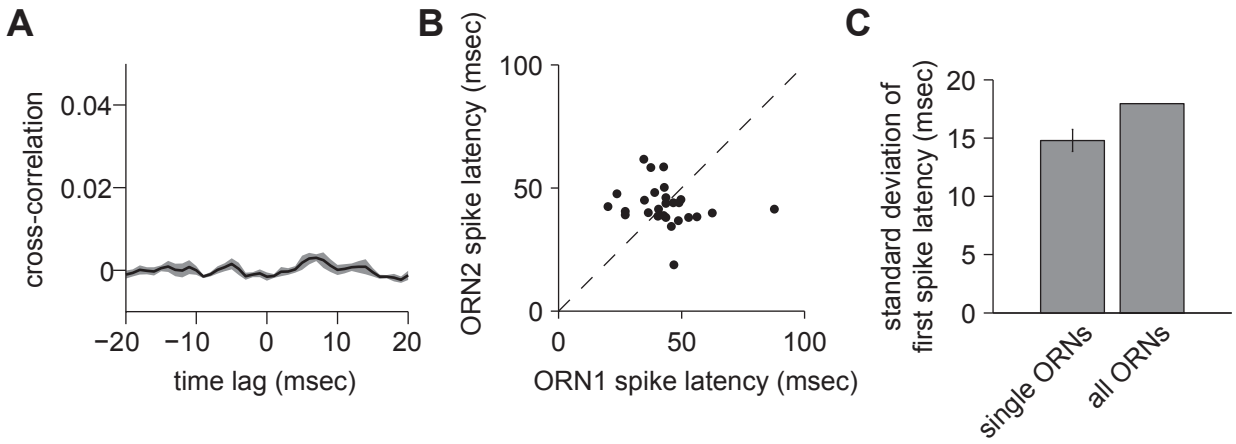

Figure S5 (Related to Figure 3). Noise in sister ORNs is not correlated and most variability in spike latency comes from within ORNs

A previous study has found that ORNs spike independently (Kazama and Wilson, 2009). To confirm this finding in DA1 ORNs, we made simultaneous paired extracellular recordings from sister ORNs (n = 6 pairs). We computed the shuffle-corrected cross correlation functions for spontaneous activity, exactly as in Figure 5F, and it was flat, indicating independence (**A**). To check for correlated fluctuations in the onset of evoked activity, we compared first-spike latencies in response to the primary stimulus used throughout this study (**B**). These latencies were not correlated between sister ORNs.

We also compared the variability in ORN first spike times within single ORNs to that within simulated populations of 40 ORNs (**C**). Most of the variability in spike latency comes from variability within ORNs. Only a small fraction comes from systematic differences between ORNs. Consequently, it is reasonable to simulate simultaneous spike trains of populations of ORNs by selecting trials randomly from our large data set of recordings from many different ORNs.

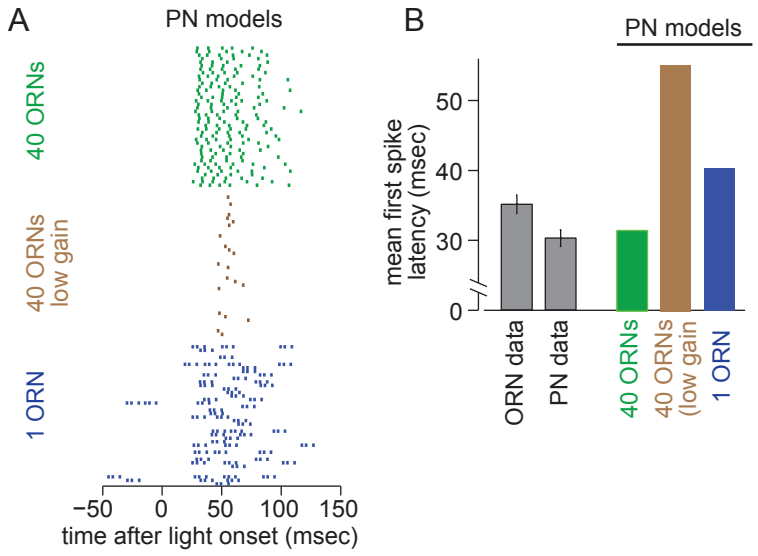

Figure S6 (Related to Figure 2). An integrate-and-fire model of a PN can reproduce the short first spike latency.

The typical PN first spike latency is actually faster than the typical ORN first spike latency (Figure 2G). Here we use a model to show that this depends critically on the fact that PNs have a low decision threshold (i.e., only a small fraction of the presynaptic ORN pool must fire a stimulus-evoked spike in order to trigger the first PN spike). The key is that a PN will spike when the fastest fraction of the ORN population has fired, although the identity of the fastest ORNs is not the same on each trial. To show that the measured integrative properties of PNs are compatible with a fast response, we constructed a simple leaky integrate-and-fire model. The model was constrained by our measurements and published data on PNs and their input synapses (see **Supplemental Experimental Procedures, Modeling**). On each trial, we randomly drew 40 ORN spike trains from our data set and fed them into the model. This model PN accurately predicted the measured fast first spike latency in real PNs. The model PN's first spike latency was lengthened when we reduced the strength of ORN-to-PN synapses, so that the effective spike count threshold was higher (model with "low gain", corresponding to a 3-fold reduction in the unitary synaptic conductance). PN first spike latency was also lengthened when we reduced the number of ORNs in the presynaptic pool, even though we proportionately increased the synaptic conductance in this case (model with 1 ORN, 40-fold increase in the unitary synaptic conductance as compared to the original model). Together, these model results illustrate how high convergence and low spike count threshold can yield an especially fast postsynaptic response. The same point has been made by experimental studies using dynamic clamp to simulate synaptic inputs (Xu-Friedman & Regehr, 2005a,b).

Xu-Friedman, M.A., and Regehr, W.G. (2005a). Dynamic-clamp analysis of the effects of convergence on spike timing. I. Many synaptic inputs. J Neurophysiol 94, 2512-2525.

Xu-Friedman, M.A., and Regehr, W.G. (2005b). Dynamic-clamp analysis of the effects of convergence on spike timing. II. Few synaptic inputs. J Neurophysiol 94, 2526-2534.

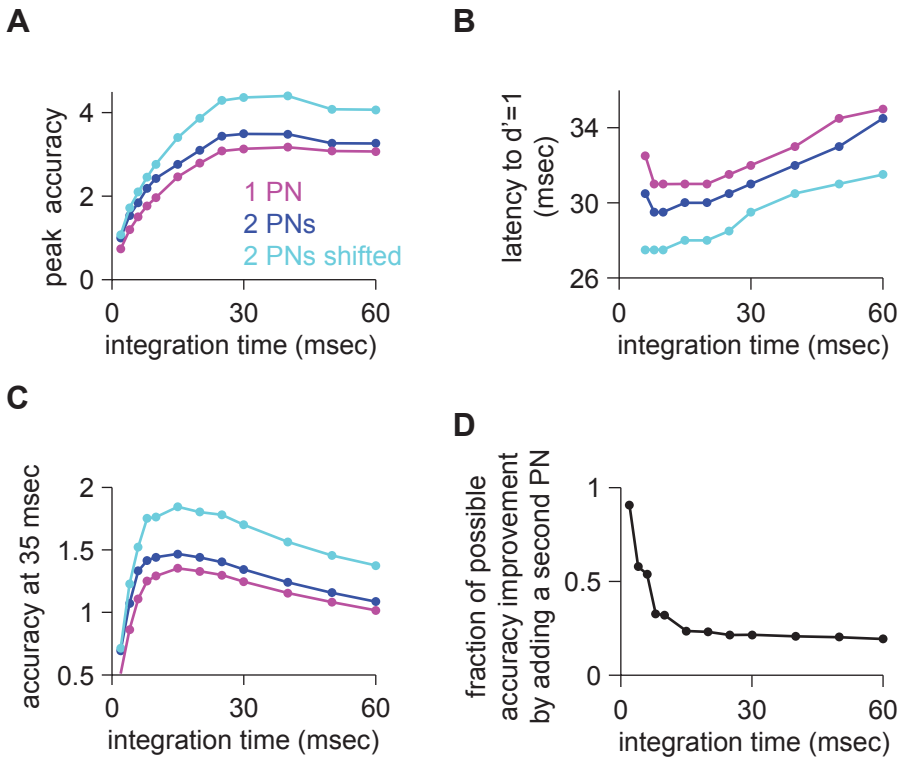

Figure S7 (Related to Figure 6). Noise correlations between PNs are timescale-dependent

Trial-to-trial variability between PNs is correlated. These "noise" correlations can limit decoding accuracy between PNs (Zohary et al., 1994). To determine the degree to which these correlations affect accuracy and latency of stimulus detection by a decoder of PNs, we shifted the trial order between simultaneously-recorded PNs and repeated the analyses of Figure 6C-E (corresponding to panels **A-C** here). This manipulation eliminates noise correlations while maintaining the trial-averaged single neuron responses. Comparing shifted and unshifted PN pairs, we find that noise correlations always decrease accuracy (**A,C**) and increase latency (**B**), as expected.

The effects of noise correlations on accuracy depend on integration time: for shorter integration times, noise correlations have little impact, whereas for longer integration times, noise correlations have a much larger impact (**A,C**). To quantify the timescale dependence of the effects of noise correlation on detection accuracy, we computed the fractional improvement in accuracy at 35 msec (**D**). Because signal and noise both arise from the same source (convergent ORN input), correlated noise can only impair detection accuracy (Averbeck, et al., 2006). Thus we can consider the shifted PN pair as an upper bound on the accuracy attainable by 2 PNs. The fraction of the total improvement possible (relative to a single PN) can then be computed as $(\text{accuracy}_{2PN} - \text{accuracy}_{1PN})/(\text{accuracy}_{2PN,shifted} - \text{accuracy}_{1PN})$. This indicates that noise correlations have less impact on accuracy for short integration times (shorter than ~12 msec). We estimate that LHNs, the "true" biological decoders of PNs, have integration times of 8-12 msec, and thus benefit from a relatively small effect of noise correlations (Figures 7,8). Note that this effect of the timescale-dependence of noise correlations can also be seen in the simulations of 3-6 PNs in Figure 6F. This effect leads to the peak accuracy occuring at a shorter integration time for 6 PNs than for 1 PN.

Averbeck, B.B., Latham, P.E., Pouget, A., Neural correlations, population coding and computation. *Nat. Rev. Neurosci*. 7, 358-366.
Zohary, E., Shadlen, M.N., Newsome, W.T., Correlated neuronal discharge and its implications for psychophysical performance. *Nature* 270, 140-143.

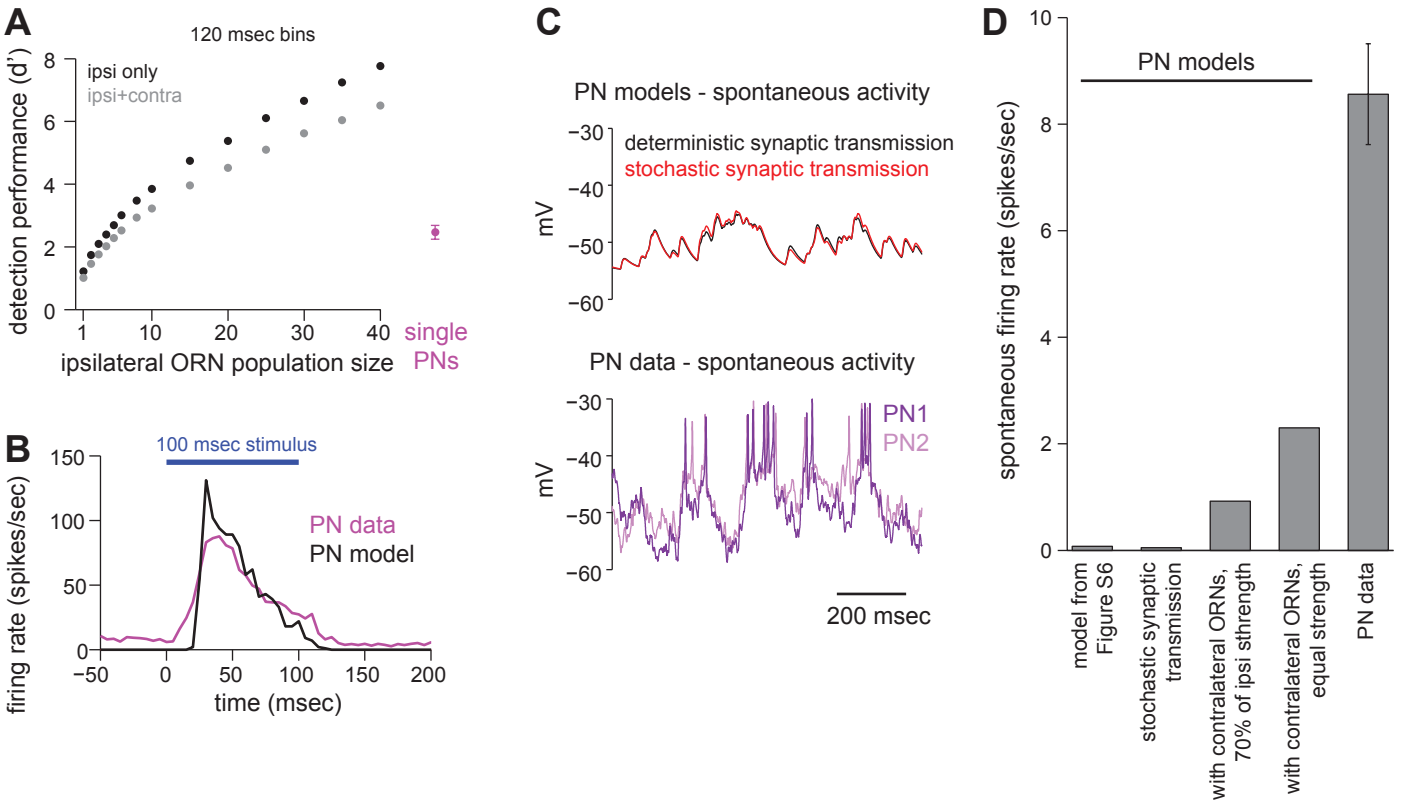

Figure S8 (Related to Figure 4). Spontaneous PN activity is not entirely due to feedforward ORN input

If PNs pooled ORN input linearly and noiselessly, we would expect PN detection performance to be similar to the performance of a pool of 40 ORNs. However, PN performance is actually lower, equivalent to the performance of only about 4-5 ORNs (**A**, black points). (Here we pool ORNs as in Figure 3, by randomly drawing individual trials from our large data set of ORN spike trains, and we measure stimulus detection performance using the d′ metric.)

What is the source of this discrepancy? A model PN which simply linearly sums the spike trains of 40 ORNs (at the level of synaptic conductances) clearly under-predicts the noise in real PN spike trains. This type of model is shown in **Figure S6**. The only noise in this model is the noise in ORN spike trains. This model under-predicts spontaneous firing rates in PNs (**B**). It also under-predicts trial-to-trial fluctuations in PN spike timing and spike counts.

We used this model as a way to explore potential explanations for the added noise in PNs. First, we ask whether variability in EPSP amplitude due to stochastic presynaptic vesicle release might account for the low spontaneous rates. To simulate stochastic release, we modeled EPSP amplitude as a binomial distribution based on 30 presynaptic vesicle release sites (Kazama and Wilson, 2008) and a release probability (p) of 0.5, which is the value of p which maximizes synaptic noise. Modeling PNs in this manner did not dramatically change the predicted voltage fluctuations (**C**, top). In real PNs, voltage fluctuations were considerably larger than those predicted by this model (**C**, bottom).

Second, we ask whether the model's low predicted spontaneous rate might result from only modeling ipsilateral ORN input. The DA1 glomerulus, like most glomeruli, receives bilateral ORN input from both antennae. However, ORNs from the contralateral antenna have about 30% lower synaptic efficacy than do ORNs from the ipsilateral antenna (Gaudry et al., 2013). To model these inputs, we added to our model 40 "contralateral" ORNs having a synaptic conductance which is 30% smaller than that at "ipsilateral" synapses. This addition increased the model PN's spontaneous rate, but only slightly (**D**). As an upper bound, we also considered a situation where contralateral ORN synapses were as strong as ipsilateral synapses. In this case, the increase in the model PN's spontaneous rate was larger, but still short of the true PN spontaneous rate (**D**). Including a pool of 40 contralateral ORNs had little effect on the performance of simulated ORN pools (**A**, gray points); they decrease performance slightly because the contralateral ORNs are not stimulated with light, and we modeled them using spike train data recorded in the absence of any stimulus.

These simulations reveal that two feedforward sources of variability, synaptic noise and contralateral ORN input, cannot fully account for the observed rates of PN spontaneous activity in our data. Because PN spontaneous spike rates drop to zero without ORN input (Gouwens and Wilson, 2009), the additional noise in PNs likely depends on neurons which are themselves driven by ORNs, such as local interneurons in the antennal lobe.

Supplemental Experimental Procedures

Fly Stocks

Flies were raised on conventional cornmeal agar medium supplemented with rehydrated potato flakes (Carolina Biological Supply) under a 12 h light, 12 h dark cycle at 25°C. Four to six hours after eclosion, flies were transferred to small vials containing rehydrated potato flakes and 100 µL of all-*trans*-retinal stock solution (Sigma; 35 mM in ethanol). All experiments were conducted on adult male flies within 24-48 hours after eclosion. The genotype used for nearly all experiments was *Mz19-Gal4,UAS-CD8:GFP;JK1029-VP16-AD,ChaDBD/UAS-ChR2-YFP*. *Mz19-Gal4* drives expression in DA1 PNs (Tanaka et al., 2004). *JK1029-VP16-AD,ChaDBD* drives strong expression in several clusters of LHNs receiving DA1 PN input (Kohl et al., 2013), as well as strong expression in DA1 ORNs. The number of Gal4-expressing ORNs was assessed by visualizing GFP expression in the distal antennal segment and counting labeled somata. We observed about 40 labeled ORNs, each of which typically extended a dendrite into a trichoid sensillum. This value is within the range of published estimates (of 20-55 ORNs; Shanbhag et al., 1999; Venkatesh and Singh, 1984).

Some of the PN-LHN paired recordings (6 of 22) were conducted in flies lacking channelrhodopsin (genotype *Mz19-Gal4,UAS-CD8:GFP;JK1029-VP16-AD,ChaDBD/+*) and one PN-LHN paired recording was conducted in a fly of genotype *10xUAS-IVS-mCD8:GFP;fru-Gal4*. In addition, some control experiments described below were carried out in flies lacking channelrhodopsin.

Anti-CD8 immunofluorescence and confocal microscopy revealed that *JK1029-VP16-AD,ChaDBD* drives much weaker expression in several other ORN types (DC3, DC4, VA1d, VA6, DM6, DM5, DC1, and VC3; data not shown). Expression in DA1 ORNs is much stronger (which is why only 40 ORNs are visible in the antenna and why only DA1 fluorescence is visible in the images shown in Kohl et al., 2013). Levels of

channelrhodopsin expression in these off-target ORNs are too weak to drive light-evoked responses. We verified this in pilot studies by performing recordings from a sample of off-target ORN types that are accessible to electrophysiological recording (DC3, VA1d, DM5, and DC1). We found no spiking responses to any stimuli featured in this study, except for the VA1d ORNs, which responded weakly to the strongest stimulus in Figure 1C,D. Thus, essentially all the responses of PNs and LHNs in this study must be driven exclusively by the activity of DA1 ORNs.

Transgenic stocks (other than those cited above) have been previously published as follows: *UAS-ChR2-YFP* (Hwang et al., 2007), *Mz19-Gal4* (Tanaka et al., 2004), *UAS-CD8:GFP* (Lee and Luo, 1999), *10xUAS-IVS-mCD8:GFP* (Pfeiffer et al., 2010), *fru-Gal4* (Demir and Dickson, 2005).

Electrophysiology

In vivo extracellular ORN recordings were performed as described previously (Wilson et al., 2004), with the exception that sharp electrodes were fabricated from quartz glass (Sutter; 1.0 mm outer diameter, 0.7 mm inner diameter) using a laser puller (Sutter) to facilitate penetration of the tough cuticle surrounding DA1 ORNs. DA1 ORNs are housed in the at1 trichoid sensilla on the surface of the antenna; at1 is the only sensillum that houses exactly 1 ORN (Clyne et al., 1997; van der Goes van Naters and Carlson, 2007). DA1 ORNs were identified on the basis of sensillum morphology, the presence of spikes with only one characteristic amplitude and shape, a low spontaneous spike rate, and responsiveness to *cis*-vaccenyl acetate.

In vivo whole-cell patch clamp and cell-attached PN and LHN recordings (including simultaneous PN-LHN recordings, Figure 5) were performed as described previously (Fisek and Wilson, 2014). The internal patch pipette solution contained (in mM): 140 potassium aspartate, 10 4-(hydroxyethyl)-1-piperazineethanesulfonic acid (HEPES), 4 MgATP, 0.5 Na_3GTP, 1 ethylene glycol tetraacetic acid, 1 KCl, and 13 biocytin hydrazide.

(pH 7.2, osmolarity adjusted to ~265 mOsm). The external saline contained (in mM): 103 NaCl, 3 KCl, 5 N-tris(hydroxymethyl) methyl-2-aminoethane-sulfonic acid, 8 trehalose, 10 glucose, 26 $NaHCO_3$, 1 NaH_2PO_4, 1.5 $CaCl_2$ and 4 $MgCl_2$. The osmolarity was adjusted to 270–273 mOsm. The saline was bubbled with 95% O_2 and 5% CO_2 and reached a final pH of 7.3.

PN recordings were performed with patch pipettes made from borosilicate glass with thick wall (Sutter; 1.5 mm outer diameter, 0.86 mm inner diameter) or thin wall (World Precision Instruments; 1.5 mm outer diameter, 1.12 mm inner diameter). LHN recordings were performed exclusively with thick wall pipettes. For all LHN recordings and some PN recordings, the patch pipette tip was pressure-polished with a microforge (ALA scientific instruments) to achieve lower resistance. Pipette resistances ranged from 7-15MΩ. All recordings were obtained with Axopatch 200B model amplifiers with CV-203BU headstages and were acquired with custom-written MATLAB routines. Whole-cell recordings were made in current-clamp mode, low-pass filtered (5 kHz cutoff frequency), digitized (10 kHz) and stored for offline analysis. Cell-attached recordings were made in voltage-clamp mode, low-pass filtered (1 kHz cutoff frequency), digitized (10 kHz) and stored for offline analysis.

Pipettes were prepared for cell-attached recordings by gently pushing the pipette tip into an unrelated contralateral neuropil prior to contacting the soma of interest; this reduced the seal resistance in cell-attached mode and thus the likelihood of inadvertently breaking into the cell. For most cell-attached recordings, the pipette was filled with external saline instead of internal saline (for the remainder, the pipette was filled with internal saline). The voltage command in the cell-attached recordings was adjusted so that the net current passing the electrode was close to zero. For whole-cell recordings, a small amount of hyperpolarizing current was applied to offset the ~10 mV depolarization caused by the pipette seal conductance (Gouwens and Wilson, 2009) and to match the spontaneous rate of extracellular spikes observed prior to breaking in to the cell as precisely as possible. In cases where extracellular spikes were not visible (more common in LHN recordings),

hyperpolarizing current was applied so that spontaneous spiking resembled that of other cell-attached recordings from that cell type.

DA1 PNs were identified as the only PNs in *Mz19-Gal4* with somata in the lateral cluster (Zhu and Luo, 2004). LHNs in this study were identified by the anterodorsal somata position and by morphological (from biocytin fills) or physiological criteria. These LHNs correspond to a single subtype of the cluster aSP-f (Kohl et al., 2013), also known as aSP5 (Yu et al., 2010) and DC1 (Ruta et al., 2010). See Figure S1 and Figure S2 for details on LHN subtype classification and identification.

Optogenetic Stimulation

The optogenetic stimulus consisted of a blue light (470 nm) emitted by a high-power LED (ThorLabs, M470F1; 1000 mA maximum power) coupled to a 50-cm long, 200-µm core diameter optical fiber (ThorLabs, FG200LCC). LED output was controlled by a 1000 mA voltage-controlled current source (BuckPuck, LEDdynamics, Inc.). The end of the fiber was coupled to a fine cannula (105 µm core diameter, 20mm long; ThorLabs, FG105LCA) that was precisely aligned to point at the antenna ipsilateral to the recorded neuron. The contralateral antenna was not stimulated. Alignment was performed under visual guidance with two cameras (Point Grey Research) attached to magnifying lenses (Infinistix). Nearly identical alignment between preparations was achieved with fiduciary markings superimposed on the live camera images. Control experiments that systematically varied the position of the cannula showed no effect of position at the spatial scales of alignment variability likely to be present between preparations. The voltage of the LED command and the duration of the command were titrated empirically to generate a panel of different stimuli of varying duration and luminance (see Figure S3 for details).

Additional control experiments ruled out two possible unintended consequences of light in our experiments. First, it was possible that scattered light from the LED could directly excite PNs (which are closer to the antennae than LHNs are, and so more subject to this concern). PN recordings in the presence of 1µM tetrodotoxin in the external saline revealed no detectable depolarization due to the light stimulus, indicating that any scattered light that might enter the head capsule in our experimental configuration is not sufficient to directly activate PNs. Second, it is possible that LHNs could receive direct input from visual neurons. Some LHNs in locusts are multimodal, responding to both olfactory and visual stimuli (Gupta and Stopfer, 2012). The LHNs in this study have dendrites that interdigitate with processes of visual neurons (Ruta et al., 2010). However, control experiments in flies lacking channelrhodopsin (*Mz19-Gal4, UAS-CD8:GFP ; JK1029-VP16-AD, ChaDBD / MKRS*) revealed no effects of our stimulation protocol on LHN membrane potential via visual system pathways.

We also performed a control experiment to test whether expression of channelrhodopsin changes spontaneous spike rates. We found that flies lacking channelrhodopsin (*Mz19-Gal4,UAS-CD8:GFP;JK1029-VP16-AD,ChaDBD/TM6b)* had spike rates that were not significantly different from spike rates in experimental flies (i.e., the flies with channelrhodopsin used throughout this study). In ORNs, spontaneous spike rates were 1.5±1.1 spikes/sec (mean ± SD, n = 58) with channelrhodopsin and 1.6±1.8 spikes/sec (n = 7) without channelrhodopsin. In PNs, spontaneous spike rates were 8.6±6.3 spikes/sec (n = 44) with channelrhodopsin and 8.3±7.1 spikes/sec (n = 5) without channelrhodopsin.

Our aim in designing our optogenetic stimulation protocols was to create a well-controlled near-threshold stimulus for ORNs. We note that the relationship between ORN and PN firing rates has been previously characterized for strong and prolonged stimuli (in contrast to the weak and transient stimuli we use here). The ORN-PN input-output curve was previously found to be strongly sublinear, and the response was more transient in PNs than in ORNs (Bhandawat et al., 2007; Kim et al., 2015; Olsen et al., 2010). Strong and prolonged

stimuli elicit depression at ORN-to-PN synapses, as well as lateral inhibition between glomeruli (Kazama and Wilson, 2008; Olsen and Wilson, 2008; Root et al., 2008). These two mechanisms should be essentially absent in our study, because our stimuli elicit only one or two spikes per ORN, and only one glomerulus is receiving ORN input. Accordingly, the ORN-to-PN output curve we describe here is a linear one (Figure 1C), and PN responses are more prolonged than ORN responses are (Figure 1E, G).

Spike Detection

Spikes were detected using custom-written MATLAB routines. For ORN recordings, raw voltage traces were high-pass filtered with a digital 2^{nd}-order Butterworth filter with a cutoff frequency of 15 Hz, and then smoothed with a 7-point Hanning window. Spikes were detected based on threshold crossings of this filtered signal. Every trace was inspected visually to correct for omitted and erroneously-identified spikes (both of which were rare). Because ORN spike waveforms can be broad, the spike time was defined as the (negative) peak of the first derivative, the shortest-latency reliable indicator of a spike. We note that for analyzing the speed enhancement between ORNs and PNs, this procedure is the most conservative estimate of ORN spike times possible. For PN and LHN whole-cell recordings, a similar procedure was applied: we defined the spike time as the peak of the first derivative of the voltage waveform. In cell-attached recordings, spike waveforms are much narrower (<1 msec) than the waveforms of whole-cell spikes, so spike times were defined by the peak of the current waveform. LHN spikes recorded in current clamp can be, in some cases, rather low-amplitude (Fisek and Wilson, 2014; Kohl et al., 2013; Ruta et al., 2010). Thus, in practice, spike identification was assisted by detecting the transients in the current output from the Axopatch 200B amplifier. Spikes identified this way were always cross-checked with the voltage trace. For all recordings, uncertainty in spike time identification is estimated to be less than 1 msec.

Data Inclusion

We omitted from analysis all cell-attached recordings in which spikes could not be reliably identified from noise, or in which we noted signs that the patch had been ruptured (as indicated by a monophasic spike shape and a DC offset during sustained spiking). Cell-attached recordings should provide the gold standard for evaluating spontaneous spike rates, because they are unaffected by the seal conductance, which tends to depolarize small neurons recorded in whole-cell mode (Gouwens and Wilson, 2009). Three whole-cell PN recordings were omitted because their spontaneous rate was more than two standard deviations above the mean of the distribution of spontaneous rates obtained from cell-attached recordings. These high spontaneous rates likely occurred because we injected an insufficient amount of constant hyperpolarizing holding current to counteract the effect of the seal conductance (see above). Two whole-cell PN recordings were omitted due to abnormally low stimulus-evoked firing rates (i.e., no stimulus evoked more than a spike or two). This likely occurred due to damage to the antennal nerve during the dissection.

Data Analysis

Input-output curves: For the input-output curves in Figure 1C-D, the duration of the light stimulus ranged from 20 msec to 100 msec (see Figure S3). For shorter stimuli (20-30 msec) we computed firing rates over 60 msec windows starting at stimulus onset. For the long stimulus (100 msec) we computed firing rates over 120 msec windows starting at stimulus onset. These windows were chosen based on the duration of the spiking responses to these stimuli.

First spike latency: Spike latency measurements were made relative to the time onset of the voltage command to the LED. Trials in which no spike occurs within 100 msec of stimulus onset are omitted from this analysis. In practice this fraction is small for ORNs (27% of trials) and very small for PNs (6% of trials) and LHNs (9%). Because PNs have high rates of spontaneous activity, in a handful of cases the first spike measured this way

may be a "spontaneous" spike (i.e. not evoked by the stimulus). If we instead measured spike latency from 10 msec after stimulus onset (rather than measuring from the time of stimulus onset), none of the main conclusions of this study were changed. We also tested an alternative measure of spike latency that involved computing a cumulative spike count after stimulus onset, and subtracting the cumulative spike count based on epochs of spontaneous activity. This latter metric rigorously controls for spontaneous firing rate, but it also did not change any of the main conclusions of the study. Finally, none of our major conclusions changed if we measured median first spike latencies rather than mean first spike latencies.

Separation between spontaneous and evoked firing rates (stimulus detection accuracy, or *d′*): Separation between light-driven and spontaneous spike counts was computed using the metric *d′*, which is the difference in mean of the two distributions normalized by the mean of the two standard deviations:

$$d' = \frac{\mu_{driven} - \mu_{spontaneous}}{\sqrt{\frac{1}{2}\left(\sigma^2_{driven} + \sigma^2_{spontaneous}\right)}}$$

The stimulus-evoked spike count distribution was computed over sliding (overlapping) windows (with 1 msec increments) that spanned the duration of the response (Doron et al., 2014). Spontaneous spike count distributions were constructed from multiple non-overlapping windows (of the same size as used for the stimulus-evoked distributions) covering 1000 msec of spontaneous activity in each trial. Detection performance can also be analyzed using the receiver-operator characteristic (ROC) curve; repeating all of our analyses using this metric did not alter any of our conclusions. For analyses of decoder integration time in Figure 3A-D and Figure 6A-F (using the *d′* metric), the size of the window used to count spikes was varied from 2 msec to 60 msec. In Figure 3C,D, ORN populations of size K = 1 to 40 were simulated. A single trial consisted of spikes elicited by a random selection (without replacement) of K trials from the complete set of trials from each ORN recorded individually (a total of 2014 trials concatenated from our full set of 58 individual ORN recordings). This process was repeated to generate 40 trials for each pool size (replacing all trials between each repeat and pool size). This whole procedure was then repeated 50 times and averaged for each pool size to generate the

values in Figure 3C,D. This construction is justified because noise in ORNs is independent (i.e. ORNs have zero noise correlations; Figure S5; Kazama and Wilson, 2009). Because noise in sister PNs is correlated, most of the PN decoding analysis is restricted to data from our paired recordings.

Binary classifier analysis: For analyses of decoder threshold in Figure 3E-F and 6G-H, an explicit spike count threshold was added to the spike count distributions described above. For each threshold (number of spikes in a particular time window), the hit rate (correct detection of a stimulus) and false alarm rate (incorrectly detecting a stimulus when none was present) were determined. Detection latency was assessed as the first time during the stimulus period when the number of spikes in the decoding window surpassed threshold.

Correlations: Cross-correlation functions (Figure 5F) were computed using 2 msec bins spanning 1000 msec of spontaneous activity and either 120 msec or the first 35 msec of evoked activity. Correlation functions (which were shift-corrected) were calculated exactly as described previously (equations 1 and 2 in Kazama and Wilson, 2009). The range of time lags in our correlation functions (10 msec) was in one case (Figure 5F, right) of the same magnitude as the total time window of analysis (35 msec). To avoid reducing the overlap between the two binned spike rate vectors, which could distort the correlation function if it were substantial, we used the following procedure. When we computed lags other than zero, we simply shifted the entire 35-msec analysis window by the specified lag, so that correlations were always computed between pairs of 35-msec snippets. This means that the entire time epoch subject to analysis was 55 msec (35 msec + 10 msec on either side). We normalized the correlation function by the standard deviation values computed over this entire 55 msec window (equation 2 in Kazama and Wilson, 2009). Thus, for lags other than zero, the correlation values are partly dependent on spikes that occur slightly beyond the first 35 msec of activity. However, restricting all analysis to the 35 msec window yielded qualitatively similar results. In some cross-correlation functions, the peak is slightly offset from zero. This is due in part to the fact that we assigned the identity of the two PNs such that the offset is always in the same direction in every experiment. This causes the average across experiments to more

closely resemble the result of individual experiments. Correlation for varying integration windows (also shift-corrected; Figure 5G) was computed with the Pearson product moment correlation coefficient on spike counts computed within the specified window size. For integration window sizes shorter than 35 msec, there are multiple integration windows per trial; spike counts were concatenated to form a single vector (per window size) for each neuron within each pair.

Spike threshold: Spike threshold was defined as the voltage immediately preceding each spike. The rate of depolarization preceding the spike was defined as the instantaneous time derivative of the voltage at that time. These values correspond to the minimum immediately preceding the stereotyped spike trajectory in space defined by V and dV/dt (the phase portrait, Figure 7E). These values were detected as the inflection point of the voltage trace (i.e. the time where $d^2V/dt^2 = 0$) immediately preceding each spike. In cases of especially high spike rates (typically greater than ~200 Hz), subsequent spike waveforms can overlap with each other, impairing the estimation of spike threshold. These spikes were omitted from our analysis by ignoring any spike threshold that occurred with a negative dV/dt (i.e. when the rate of measured depolarization, as measured at the soma, is determined by the falling phase of the preceding spike, rather than subthreshold activity). For seven PNs, a small number of additional high frequency spikes remained, which were manually removed from further threshold analysis. For the dynamic threshold analysis, we compared the threshold of the first stimulus-evoked spike with thresholds for spontaneous spikes.

Linear filter relating ORN and PN firing rates: Because PN responses are more prolonged than ORN responses (Figure 4A), the linear filter that describes their relationship would be strictly positive (i.e., an integrating filter). Because our hypothetical decoder counts spikes in a rectangular (binary) window, we explored positive rectangular (binary) filters with different widths. Rectangular filters of various time widths were convolved with the mean time-varying ORN firing rate (in Figure 1E). We selected the filter that yielded the best approximation of the mean PN firing rate (in Figure 1E). A linear filter is a good description of the ORN-to-PN transformation because our stimulus sits within the linear regime of the ORN-to-PN gain curve (Figure 1C), because the

number of convergent ORNs is large, because ORN noise is independent (Figure S5), and because the PN threshold is relatively low.

Simulating Populations of >2 PNs

In Figure 6F, we extrapolated from paired PN recordings to populations of 3-6 PNs by modeling spike counts as correlated distributions. The modeled marginal spike count distributions followed the empirical single PN spike count distributions for each pair. Correlated activity was modeled by setting the off-diagonal terms in the covariance matrix to the empirical covariance between the two neurons. Spike counts were simulated using established methods (Macke et al., 2009). This allowed us to simulate spike counts from populations of up to 6 PNs.

In Figure 6I, populations of 6 PNs were simulated by extrapolating from pairwise correlations among PNs. The first spike latency of 2 of the 6 PNs were taken directly from data. We then computed the distribution of times between the first spike in each PN of the recorded pair. We then randomly sampled from this distribution, alternately adding or subtracting this sampled time from the empirically measured first spike latencies to build a 6-element vector of first spike latencies. This method yielded simulated spike latencies with correlations closely matched to empirical values. To simulate populations without correlations, we repeated this analysis after shifting trials in each of the recorded pairs.

PN Integrate-and-fire Model

PN activity was modeled in Figure S6 and Figure S8 using a single-compartment leaky integrate-and-fire model with conductance-based synapses, following the conventions of Yim et al. (2014). The subthreshold dynamics of the membrane potential (V_m) obey the equation

$$C_m \frac{dV_m(t)}{dt} + \frac{1}{R_m}(V_m(t) - V_{rest}) = G_{syn}(t)(V_m(t) - V_{rev}).$$

C_m denotes the membrane capacitance, R_m is the membrane resistance, V_{rest} is the resting potential. Input to the model is in the form of synaptic conductance G_{syn}. The corresponding synaptic current reverses at V_{rev}.

Only the feedforward (excitatory) synapses from ORNs are modeled. Because noise in ORNs is independent, we could model the simultaneous activity of the complete population of 40 ORNs by randomly selecting 40 single trial spike trains (without replacement) from our complete ORN dataset. These 40 spike trains were then pooled and convolved with a waveform representing the unitary excitatory postsynaptic conductance (the EPSG waveform) to generate the total synaptic conductance:

$$G_{syn} = \sum_k g_{syn}(t - t_k)$$

where t_k denotes the time of the k^{th} ORN spike providing input to the model PN. The EPSG waveform ($g_{syn}(t)$, the time course of the conductance change in response to a single ORN spike) was modeled as an alpha function:

$$g_{syn}(t) = \begin{cases} J\frac{t}{\tau}e^{1-\frac{t}{\tau}} if\ t \geq 0 \\ 0 \qquad if\ t < 0 \end{cases}$$

where J is the peak synaptic conductance and τ is the characteristic synaptic conductance timescale. ORN spike input to the model was simulated from recorded spike trains.

Parameters were based on previously published measurements (Gouwens and Wilson, 2009; Kazama and Wilson, 2008) and were assigned the following values:

Intrinsic parameters	
Membrane resistance, R_m	0.3 GΩ
Membrane capacitance, C_m	0.117 pF
Resting potential, V_{rest}	-55 mV
Spike threshold	-40 mV
Spike reset potential	-55 mV
Refractory period	2 ms
Synaptic parameters	
EPSG timescale, τ	3 ms
EPSG peak amplitude, J	0.7 nS
Synaptic reversal potential, V_{rev}	0 mV

Some of these values (R_m, C_m , J) were altered slightly from published values (0.4 GΩ, 0.135 pF, 0.54 nS, respectively) in order to maximize the qualitative fit to the data in the present study (Gouwens and Wilson, 2009). The differential equation for voltage was integrated numerically using the Euler method with a time step of 0.1 msec. When the voltage reached spike threshold, a spike was recorded, and the voltage was instantaneously set to its reset potential. The voltage was then clamped at reset for a 2 msec refractory period. These parameters produce a unitary excitatory postsynaptic potential (EPSP) of about 2 mV. It is difficult to accurately measure EPSP amplitude *in vivo* because there are many DA1 ORNs, and thus spontaneous EPSPs arising from different ORNs tend to summate and obscure the amplitude of individual events. However, an average amplitude of 2 mV appears reasonable, based on visual inspection of spontaneous EPSPs. Because these model parameters produced the best fit to PN spiking data overall, we took 2 mV as the amplitude of a unitary EPSP in generating Figure 4C, but if we assume a larger unitary EPSP (following Kazama and Wilson,

2008) our conclusions are not qualitatively different. In Figure S6, to simulate a PN with a single ORN input, the peak EPSG amplitude was increased by a factor of 40 to keep total synaptic conductance constant. To simulate a PN with a "low" gain of 1, the EPSG peak amplitude, *J*, was reduced by a factor of 3.

Statistics

To maximize statistical power, parametric statistical tests were used wherever data were normally distributed. Normality was evaluated with a Kolmogorov-Smirnov Test with $\alpha = 0.05$. When data were not normally distributed, a nonparametric test was used. The only exceptions to this were cases where we applied ANOVA or ANCOVA tests regardless of whether the data were normally distributed.

References for Supplemental Experimental Procedures

Bhandawat, V., Olsen, S.R., Schlief, M.L., Gouwens, N.W., and Wilson, R.I. (2007). Sensory processing in the Drosophila antennal lobe increases the reliability and separability of ensemble odor representations. Nat Neurosci 10, 1474-1482.

Clyne, P., Grant, A., O'Connell, R., and Carlson, J.R. (1997). Odorant response of individual sensilla on the Drosophila antenna. Invert Neurosci 3, 127-135.

Demir, E., and Dickson, B.J. (2005). fruitless splicing specifies male courtship behavior in Drosophila. Cell 121, 785-794.

Doron, G., von Heimendahl, M., Schlattmann, P., Houweling, A.R., and Brecht, M. (2014). Spiking irregularity and frequency modulate the behavioral report of single-neuron stimulation. Neuron 81, 653-663.

Fisek, M., and Wilson, R.I. (2014). Stereotyped connectivity and computations in higher-order olfactory neurons. Nat Neurosci 17, 280-288.

Gouwens, N.W., and Wilson, R.I. (2009). Signal propagation in Drosophila central neurons. J Neurosci 29, 6239-6249.

Gupta, N., and Stopfer, M. (2012). Functional analysis of a higher olfactory center, the lateral horn. J Neurosci 32, 8138-8148.

Hwang, R.Y., Zhong, L., Xu, Y., Johnson, T., Zhang, F., Deisseroth, K., and Tracey, W.D. (2007). Nociceptive neurons protect Drosophila larvae from parasitoid wasps. Curr Biol 17, 2105-2116.

Kazama, H., and Wilson, R.I. (2008). Homeostatic matching and nonlinear amplification at genetically-identified central synapses. Neuron 58, 401-413.

Kazama, H., and Wilson, R.I. (2009). Origins of correlated activity in an olfactory circuit. Nat Neurosci 12, 1136-1144.

Kim, A.J., Lazar, A.A., and Slutskiy, Y.B. (2015). Projection neurons in antennal lobes signal the acceleration of odor concentrations. eLife 4.
Kohl, J., Ostrovsky, A.D., Frechter, S., and Jefferis, G.S. (2013). A bidirectional circuit switch reroutes pheromone signals in male and female brains. Cell 155, 1610-1623.
Lee, T., and Luo, L. (1999). Mosaic analysis with a repressible cell marker for studies of gene function in neuronal morphogenesis. Neuron 22, 451-461.
Macke, J.H., Berens, P., Ecker, A.S., Tolias, A.S., and Bethge, M. (2009). Generating spike trains with specified correlation coefficients. Neural Comput 21, 397-423.
Olsen, S.R., Bhandawat, V., and Wilson, R.I. (2010). Divisive normalization in olfactory population codes. Neuron 66, 287-299.
Olsen, S.R., and Wilson, R.I. (2008). Lateral presynaptic inhibition mediates gain control in an olfactory circuit. Nature 452, 956-960.
Pfeiffer, B., Ngo, T.-T.B., Hibbard, K.L., Murphy, C., Jenett, A., Truman, J.W., and Rubin, G.M. (2010). Refinement of tools for targeted gene expression in Drosophila. Genetics 186, 735-755.
Root, C.M., Masuyama, K., Green, D.S., Enell, L.E., Nassel, D.R., Lee, C.H., and Wang, J.W. (2008). A presynaptic gain control mechanism fine-tunes olfactory behavior. Neuron 59, 311-321.
Ruta, V., Datta, S.R., Vasconcelos, M.L., Freeland, J., Looger, L.L., and Axel, R. (2010). A dimorphic pheromone circuit in Drosophila from sensory input to descending output. Nature 468, 686-690.
Shanbhag, S.R., Muller, B., and Steinbrecht, R.A. (1999). Atlas of olfactory organs of Drosophila melanogaster. 1. Types, external organization, innervation, and distribution of olfactory sensilla. Int J Insect Morphol Embryol 28, 377-397.
Tanaka, N.K., Awasaki, T., Shimada, T., and Ito, K. (2004). Integration of chemosensory pathways in the Drosophila second-order olfactory centers. Curr Biol 14, 449-457.
van der Goes van Naters, W., and Carlson, J.R. (2007). Receptors and neurons for fly odors in Drosophila. Curr Biol 17, 606-612.
Venkatesh, S., and Singh, R.N. (1984). Sensilla on the third antennal segment of *Drosophila melanogaster* meigen (Diptera : Drosophilidae). Int J Insect Morphol Embryol 13, 51-63.
Wilson, R.I., Turner, G.C., and Laurent, G. (2004). Transformation of olfactory representations in the Drosophila antennal lobe. Science 303, 366-370.
Yim, M.Y., Kumar, A., Aertsen, A., and Rotter, S. (2014). Impact of correlated inputs to neurons: modeling observations from in vivo intracellular recordings. J Comput Neurosci 37, 293-304.
Yu, J.Y., Kanai, M.I., Demir, E., Jefferis, G.S., and Dickson, B.J. (2010). Cellular organization of the neural circuit that drives Drosophila courtship behavior. Curr Biol 20, 1602-1614.
Zhu, H., and Luo, L. (2004). Diverse functions of N-cadherin in dendritic and axonal terminal arborization of olfactory projection neurons. Neuron 42, 63-75.